ASQ-MPHAAS: Multi-Payload Observation System From High Altitude Airship

Shaoxing Hu, Aiwu Zhang, and Shatuo Chai

***Abstract*— One of the critical advantages of a high-altitude airship (HAA) is its ability to carry multiple-task payloads for remote sensing monitoring on the plateau. We developed a multi-payload observation system based on the HAA (ASQ-MPHAAS) for remote sensing monitoring of the Qinghai plateau. In this paper, we demonstrate the design, development, implementation of the ASQ-MPHAAS. The ASQ-MPHAAS includes two parts; one part is our HAA (ASQ-HAA380), and the other part is our multi-payload observation system (ASQ-MPOS-1). The ASQ-MPOS-1 consists of two hyperspectral push-broom imaging sensors, a multispectral imaging sensor, a high-resolution RGB camera, a video sensor, a Position and Orientation System (POS), and other components. The ASQ-MPOS-1 is installed under the ASQ-HAA380. We also introduce some key methods of data processing we propose to solve unique problems brought by HAA. Four real-world field experiments are presented in this paper to demonstrate that the ASQ-MPHAAS can capture different kinds of remote sensing data at a high spatial resolution of a few or dozen centimeters.**

***Index Terms*— Multi-payload observation, high altitude airship time synchronization, hyperspectral imaging, multispectral imaging.**

I. Introduction

MOST parts of Qinghai Province are located at altitudes over 3000-4000 m. It is challenging to observe the grassland on Qinghai plateau using common airborne platforms such as manned aircraft and UAVs. Our research group developed a new multi-payload system based on an HAA (ASQ-MPHAAS) for remote sensing monitoring of the grasslands on Qinghai plateau. The ASQ-MPHAAS includes two parts, the HAA developed by our research group, called ASQ-HAA380, and the other part is our ASQ-MPOS-1. The ASQ-HAA380 is 38 meters long and 12 meters high and can fly at an altitude of 5000m above sea level. The ASQ-MPOS-1 includes a high spatial resolution camera with a big CCD matrix, a multispectral imaging payload, two hyperspectral imaging payloads, a video sensor, and a POS (the Position and Orientation System). The ASQ-MPOS-1 is directly installed under the ASQ-HAA380 to synchronously acquire different remote sensing data. In this paper, we mainly describe the design and development of ASQ-MPOS-1 and present some data processing methods.

The ASQ-MPHAAS is a new observation platform. Compared with satellite platforms [1]–[8], the ASQ-MPHAAS can cruise and observe, hover, and stare. Its flight cost is lower than satellites, and it can provide immediate coverage for emergency management. The payload can be easily exchanged, and the senors are capable of capturing high spatial resolution images. No current satellite systems can provide such high-resolution imagery. For example, the spatial resolution of TM [5] images are 30 meters, useful for interpreting the main grassland types, but they cannot be used to study the species distribution of small-sized plants in the natural grassland. Although GF(Gaofen)-2 [7] carries a 4m resolution multispectral camera, the multispectral camera has only four bands; it cannot meet the demands of complex indicators monitoring. Compared with the typical manned aircraft system, the ASQ-MPHAAS is developed for the high-altitude environment monitoring; it can fly and observe at an altitude of over 5000 m above the sea level. For safety reasons, the generally manned aircraft are rarely used in remote sensing monitoring on the Qinghai plateau. Compared with the typical UAV remote sensing system [9]–[11], security, load capacity, and flight time of ASQ-MPHAAS far exceeds those of standard UAS.

Due to the limitation of load capacity, most of the airborne remote sensing systems only include a single-task payload. For example, airborne LiDAR [12]–[14], aerial camera [15], airborne hyperspectral imaging system [16] are bigger and expensive. But the ASQ-MPOS-1 employs 6 task payloads to synchronously collect different kinds of remote sensing data for multi-task indicators monitoring. In some sense, the ASQ-MPOS-1 not only meets the needs of sophisticated monitoring but also reduces the operation cost.

This paper describes the deployment of the ASQ-MPOS-1 task payloads (Section 2.1), while Section 2.2 and Section 2.3 contains an in-depth description of time synchronization and power supply of the ASQ-MPOS-1. Section 2.4 introduces the integration of the ASQ-MPOS-1 with the ASQ-HAA380 into the ASQ-MPHAAS. Characteristics of the ASQ-MPHAAS's push-broom sensor, including repeated sampling, missed sampling, and multi-scale sampling, some image processing

Manuscript received January 5, 2019; revised August 7, 2019; accepted August 15, 2019. Date of publication August 27, 2019; date of current version November 26, 2019. This work was supported in part by the grant from the National Natural Science Foundation of China (NSFC) under Grant 41571369, in part by the National Key Research and Development Program under Grant 2016YFB0502500, and in part by the grant from the Qinghai Science & Technology Program under Grant 2016-NK-138. The associate editor coordinating the review of this paper and approving it for publication was Dr. Ravibabu Mulaveesala. *(Corresponding author: Aiwu Zhang.)*

S. Hu is with the School of Mechanical Engineering and Automation, Beihang University, Beijing 100191, China (e-mail: husx98@163.com).

A. Zhang is with the Ministry of Education Key Laboratory of 3D Information Acquisition and Application, Capital Normal University, Beijing 100048, China (e-mail: zhang_aiwu@126.com).

S. Chai is with the Qinghai Academy of Animal Science and Veterinary, Qinghai University, Qinghai 810016, China (e-mail: chaishatuo@163.com).

Digital Object Identifier 10.1109/JSEN.2019.2937804

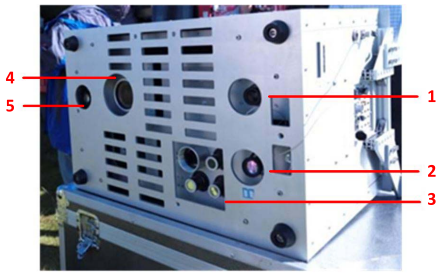

Fig. 1. The ASQ-MPOS-1. (1- VNIRHSI (the visible & near-infrared hyperspectral push-broom imaging payload); 2- SWIRHSI (the SWIR hyperspectral push-broom imaging payload); 3-MSI (the multi-spectral imaging payload consisting of 4 cameras); 4- HRI (the high resolution payload); 5- video sensor; POS and other components in the box).

methods are presented in Section 3. The band to band image registration is discussed in Section 4. In Section 5, we offer four field experiments. Experiment I demonstrates the processing flow of correcting the time errors between the POS and the hyperspectral imaging payloads. Experiment II and experiment III analyze several methods to solve the unique problems of hyperspectral push-broom imaging based on the ASQ- MPHAAS. Finally, in Experiment IV, the ASQ-MPHAAS is tested on Jinyintan grassland of Qinghai plateau, and ASQ-MPHAAS achieve centimeter-level spatial resolution. This spatial resolution was found to be adequate for capturing the plants and other objects of grassland in sufficient detail.

II. Material and Methods

A. Deployment of Task Payloads

According to the demands of multi-indicator monitoring of grasslands on the Qinghai plateau, we integrated different task payloads on the ASQ-MPOS-1, as if some different function eyes were installed on the ASQ-MPHAAS. These task payloads integrated on ASQ-MPOS-1 consist of a digital camera with a big CCD matrix, a multi-spectral imaging payload, two hyperspectral imaging payloads, a video sensor, and a POS, in Figure 1.

The multispectral/hyperspectral payloads are used to quantify the biochemical and biophysical characteristics of vegetation, water, forest, etc. The high spatial resolution camera captures high spatial resolution images that are used to detect cattle and sheep on the grassland. The video sensor monitors the ASQ-MPHAAS flight status. The POS provides position and orientation information for direct georeferencing of imaging payloads.

1) Hyperspectral Push-Broom Imaging Payload (HSI): Our hyperspectral push-broom imaging payload (HSI) is composed of loosely integrated off-the-shelf components: a hyperspectral sensor, a digital camera, and a camera lens. The hyperspectral sensor is a single linear imaging component, and each image captured by the sensor represents a line in the hyperspectral image, so the design of our HSI is referred to as a push-broom scanner. Images taken by the HSI are synchronized to the trajectory data from POS through GPS time. A detailed description of POS and GPS-based time synchronization is presented in the next sub-sections.

Several companies develop hyperspectral sensors [16], such as AisaEAGLE with 400-970nm and 488 spectral bands; AisaHAWK with 970-2500nm and 254 spectral bands; CASI with 400-1100nm and 288 spectral channel, and so on. We selected some components to develop two HSIs and integrated them on the ASQ-MPOS-1 (Figure 1): one is operated in the VNIR spectral domain, and the other is operated SWIR spectral domain.

The VNIRHSI's lens objective has a focal length of 23 mm and a field of view (FOV) of 28.9°, a VNIR Specim ImSpector [17] and a digital camera with a CCD full resolution of 1600×1200 pixels. In our implementation, we acquire 1600 pixels in the spatial dimension and 840 pixels in the spectral dimension. The finest physically feasible spectral sampling of the VNIRHSI has 840 spectral bands between 389.88-1000.78 nm, allowing a maximum frame rate of about 33 fps. The SWIRHSI's lens objective has a focal length of 22.5 mm and a field of view (FOV) of 24°, a SWIR Specim ImSpector [17] and a SWIR camera with a full resolution of 320×256 pixels. In our implementation, we acquire 320 pixels in the spatial dimension and 256 pixels in the spectral dimension. The finest physically feasible spectral sampling of the SWIRHSI is 256 spectral bands between 961.714 - 2581.48 nm, allowing a maximum frame rate of about 100 fps. The raw images of the HSI are recorded in digital counts of the 12-bit sensor range.

Before applying the HSIs in the field experiments, spectral and radiometric calibration of the HSIs were carried out. We used the methods described previously (see [18]–[20]).

2) Multi-Spectral Imaging Payload (MSI): Our research group developed a multi-spectral imaging payload (MSI) (it is shown in Figure 1), which is composed of four identical monochrome cameras and four bandpass filters. The MSI is like the Mini-MCA (Modified Tetracam Miniature Multiple Camera Array) [21]. The four identical monochrome cameras are sensitive in the 400 to 1000 nm spectral range, have the capability of obtaining 8-bit images with 1392 × 1040 pixels, allowing a maximum frame rate of about 30 fps, and are respectively equipped with near-infrared (800 nm), red (650 nm), green (550 nm) and blue (450 nm) bandpass filters. As a result, it has the flexibility to change filters to acquire other band images in the 400 to 1000 nm spectral range for specific requirements.

3) Position and Orientation System Subsystem (POS): A POS is a crucial component of ASQ-MPOS-1; it provides position and orientation information for direct georeferencing of the imaging payloads. The POS on ASQ-MPOS-1 is a SPAN-CPT GPS/INS system from NovAtel. It can achieve a positional accuracy of 0.25 m and attitude accuracy of 0.08 deg [22].

4) High-Resolution Camera and Video Camera: We selected a Hasselblad 3DII-50 camera as a high-resolution payload (HRI) with 6132×8167 pixels. We chose an industrial-grade video camera as a video payload with an image size of 1920×1080 pixels and the frame rate of about 30 fps. The images taken by the high-resolution camera are used to detect cattle and sheep on the grassland. The images captured by the video camera are sent to the based-ground

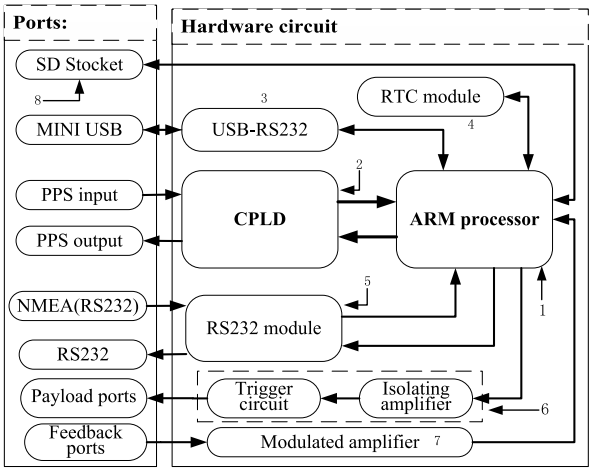

Fig. 2. The structure composition of the time synchronization control unit (1-ARM processing module, 2-CPLD processing module, 3- USB-port module, 4-RTC module, 5-RS232 module, 6-module, 7-signal modulation module, 8-SD card).

control system and to monitor the flight state of the ASQ-MPHAAS.

B. Time Synchronization Subsystem

Images taken by the different imaging payloads must be precisely synchronized to the position and orientation data from POS through a time base. However, images are captured by the imaging payloads, and the position and orientation information is measured and recorded by POS. In this study, we designed a time sync control unit and proposed a method of time sync error estimation.

1) Time Sync Control Unit: Some systems can provide a precision timebase such as GPS-based timing, IEEE 1588 Precision Time Protocol (PTP) [23], Network Time Protocol (NTP) [24], [25] and Synchronous Ethernet (SyncE) timing, and we choose GPS time base.

The GPS receiver also outputs a pulse-per-second signal (PPS) and National Marine Electronics Association (NMEA) telegrams including the GPS time with an accuracy of 15 ns at one sigma confidence level. A time sync control unit is designed to accept the PPS signal and NMEA telegrams from a GPS receiver, give a microsecond accurate time-stamping of each image frame and trigger the camera (s) to exposure at the precalculated positions. Figure 2 shows the structural composition of the time sync control unit we designed.

1-ARM processing module: accepts the information of the GPS Serial port and resolves it, computes the exposure-time interval, sends a trigger signal, checks feedback signal, reads the RTC clock information, saves data on the SD card, and so on.

2-CPLD processing module: accepts the PPS signal, and the other extended pulse signals.

3-USB-port module: exchanges data between the computer and the time sync control unit and supplies power to the time sync control unit.

4-RTC module: is an off-line clock module of the time sync control unit, when the GPS loses signal, it records the time information of the RTC clock.

5-RS232 module: reads the GPS information from the GPS receiver, outputs the extent formation of GPS, and inputs the GPS information into the other external devices.

6-Trigger module: it is an actuator of the time sync control unit. It consists of the isolating transformation circuits, amplifier circuits, and relays. It is in charge of driving the relay group closing, controlling camera exposure according to the GPS position information, making time stamps for all imaging payloads on ASQ-MPOS-1.

7-Signal modulation module: is a feedback module of the time sync control unit. It is in charge of modulating, amplifying and shaping the weak signal of exposure, etc. of the payloads, and input the processed signal to ARM.

8-SD card: is a time sync control unit recorder, and saves the data from ARM.

CPLD is one of the critical modules of the time sync control unit. CPLD waits for PPS output from the GPS receiver when it detects the rising edge of PPS. CPLD will output the timing signal into multichannel extension timing ports at the same time. Meanwhile, CPLD will reset the millisecond pulse timing port and then recount the millisecond pulses. CPLD informs ARM that the signal of PPS has been received and the millisecond pulse timing port has been reset. When the GPS signal is lost, the time sync control unit cannot receive PPS from the GPS receiver. CPLD tells ARM that GPS signal is lost and ARM needs to be changed into the RTC mode, and then CPLD outputs multichannel extension timing signal into the external devices using the RTC clock. After CPLD receives the PPS signal every time, the following occurs:

(1) It will record the value N1 of the current counter of CPLD.

(2) It will wait and receive NMEA data, extract the GPS time of PPS, it is $\mathrm{T_{pps}}$. And then the GPS time ($\mathrm{T_{gps}}$) is corresponding to the value N2 of the current counter of CPLD.

$$T_{gps} = T_{pps} + \frac{(N_2 - N_1)}{F_{frequency}} \tag{1}$$

In Equation (1), $\mathrm{F_{frequency}}$ represents the recording frequency of the counter. CPLD transfers the value of the current counter into the GPS time and gives a timestamp for each image.

2) Time Sync Error Estimation: Small timing errors occur due to a fault in synchronization between the navigation system and the imaging payloads. In other words, there is a minimal offset ($\Delta\mathrm{T_{gps}}$) between the calculated value $\mathrm{T_{gps}}$ using Equation (1) and the modified value $\mathrm{T^*_{gps}}$. The timing errors have a significant influence on direct georeferencing and georectification of the push-broom images. Assuming all of the small timing offsets are equal; we estimate the small timing offset $\Delta\mathrm{T_{gps}}$ using the method as following.

(1) consistently add a very small value Δt to $\mathrm{T_{gps}}$,

$$\overline{T^*_{gps}(i,j)} = \overline{T_{gps}(j)} + i * \Delta\mathrm{t}, \quad i = 1,2,3,\cdots,M, \quad j = 1,2,3,\cdots,N \tag{2}$$

and through M times of calculations, a time sequence $\mathrm{M \times N}$ of $\vec{T}^*_{gps}$ is formed.

(2) constantly update the corresponding between image data and POS data,

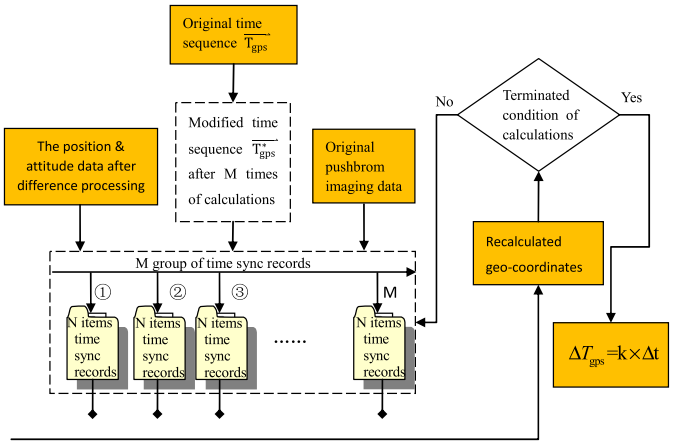

Fig. 3. The processing flow of timing sync offset estimation.

(3) constantly update the direct georeferencing coordinates of the pixels on the image, and the maximum number of calculations is M.

(4) The loop computation is terminated until a certain condition is fulfilled. The termination condition is described in Section 5.1. When the loop computation stops, if the number of computations is k, and the timing offset ΔT_{gps} is,

$$\Delta T_{gps} = k \times \Delta t \tag{3}$$

The processing flow of timing offset estimation is described in Figure 3.

C. Power Supply Subsystem

All electrical power for the ASQ-MPHAAS, including the ASQ-HAA380 and the ASQ-MPOS-1, is supplied from a hybrid energy power supply subsystem developed by our research group. The power supply subsystem consists of a power generation & storage module and a power-consumption module.

Electrical power for all of the electric devices of the ASQ-MPHAAS is supplied from the power generation & storage module. It consists of engines, generators, solar batteries, a solar controller, and storage batteries.

When the ASQ-MPHAAS takes off, the electrical energy is generated by the power generation & storage module and drives the engines to start. After the engines starts, it sets off the generators. Part of the produced electrical power is stored in batteries; the other part is sent to the electric devices of the ASQ-MPHAAS. At the same time, the solar batteries transform solar energy directly into electrical energy, and the electrical energy is transferred to the storage batteries and the electric equipment.

The power-consumption module consists of the electric devices of the ASQ-HAA380 and the electric devices of the ASQ-MPOS-1. The smallest power of the ASQ-MPOS-1 required is 610w, and the smallest power of the ASQ-HAA380 in the normal working situation is 610w. The power needs of the ASQ-HAA380 and the ASQ- MPOS-1 is shown in Figure 4.

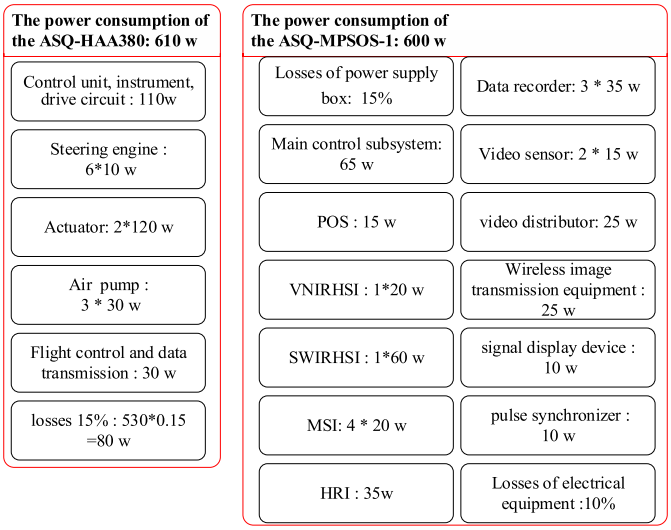

Fig. 4. The power consumption of the ASQ-HAA380 and the ASQ- MPOS-1.

Fig. 5. The ASQ-HAA380 navigated in the Qinhai Plateau with ASQ-MPOS-1.

D. HAA and Payload System Integration

Air pressure, temperature, power of hydraulic devices, and motor power are all decreasing with increasing altitude. This is especially true over a 3km altitude, where air pressure, temperature, power of hydraulic devices, and power of motors decline rapidly. Most parts of Qinghai Province is above 3500-4500m above the sea level, presenting a significant challenge for the design and development of the ASQ-MPHAAS (in Figure 5). We took the use of all-in-one design for integration of the HAA and the payload system, in addition to thinking about size and weight of the HAA, power consumption, size and weight of the payload system, etc. Below we describe how we have chosen to overcome these challenges.

(1) On the Qinghai plateau, winds are strong, and the weather unpredictable.

The size and weight of ASQ-MPHAAS are as small and light as possible under the condition of meeting the application requirements. The ASQ-MPOS-1 was designed to be lightweight and directly installed under the ASQ-HAA380 without the three-axis stabilized platform.

(2) The ASQ- MPOS-1 is a stand-alone instrument, capable of operating even when not mounted on the ASQ-HAA380. It can be done on-ground testing and calibration without the requirement for the ASQ-HAA380, and it also can be mounted on the other platforms such as airplanes or cars.

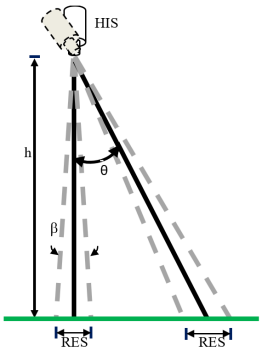

Fig. 6. To each different roll angle there corresponds a different ground resolution.

(3) All payloads have to be strengthened and mounted on a shock-absorbing deck to prevent vibration from causing image motion blur and damage to electronics. Also, the sensors have enough space between them to avoid disturbing signals.

(4) The HAA is a big soft-body aerostat, so the wave-transmitting materials are used to make the skin of ASQ-HAA380 to keep receiving GPS signal.

III. Hyperspectral Push-Broom Imaging Characteristics Based on the HAA

The hyperspectral push-broom imaging payload (HSI) was mounted on the ASQ-MPOS-1 with five other task payloads and directly installed under the ASQ-HAA380 without the three-axis stabilized platform. The pitch and roll angles of ASQ-HAA380 are severely affected by the plateau airflow. The pitch and roll angle change gravely affects the HSI, the big roll angle results in different ground resolution of each pixel of images, and the big pitch angle causes repeated and missed sampling alternatively.

In this case, how to map the geolocation data of pixels into the output grid cells is essential.

A. Multi-Scale Sampling

When the big roll angles appearing, the ground resolution is changed.

In Figure 6, β is IFOV of the imaging payload, h is the flight altitude to the ground of the ASQ-MPHAAS, θ is the roll angle, $\mathrm{RES_n}$ is the ground resolution without a big roll angle, and RES_θ is the ground resolution with a big roll angle. At this point, the ground resolution is affected by the big roll angle.

$$RES_\theta = h \cdot [\tan(\theta + \frac{\beta}{2}) - \tan(\theta - \frac{\beta}{2})] \tag{4}$$

When the flight altitude of ASQ-MPHAAS to the ground h=1000m and the pixel size is 7.4μm, the ground resolutions of different roll angles are computed and listed in Table 1. Table 1 illustrates this multi-scale sampling problem which there are ground resolutions with different roll angles appearing even at the same flight altitude.

On the other hand, the tangential airflow on the Qinhai plateau makes the pitch angle of the ASQ-MPHAAS change rapidly. The big pitch angles frequently appear, resulting in the repeated and missed samples alternatively. In Figure 7, the green lines simulate the movements of the optic axis; the repeated and missed samples are shown clearly.

TABLE I
The Ground Resolutions of Different Roll Angles

θ	Ground resolution (m)
1°	0.294614
10°	0.303681
20°	0.333541
30°	0.392699
40°	0.501895
50°	0.712830
60°	1.178097
70°	2.517780

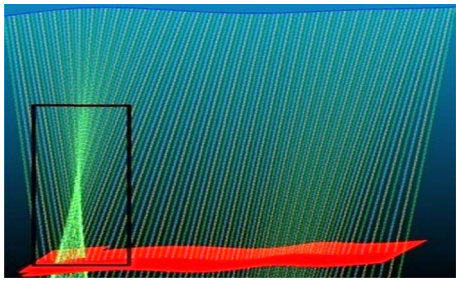

Fig. 7. The repeated and missed samples due to the big pitch angles.

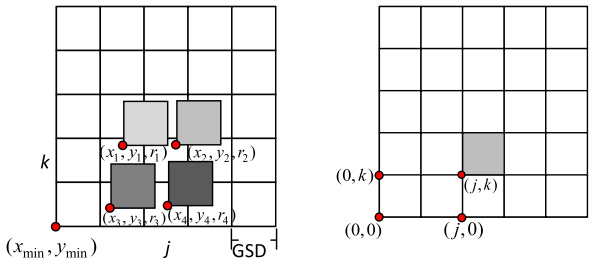

Fig. 8. The principle of linear mixed resampling model ((a) geo-coordinates, scale, and DN value before resampling; (b) DN value after resampling).

B. Linear Mixed Resampling Model

Gridding is to construct the regular grid based upon the X, Y geolocation data of the pixel, and the ground sample distance (GSD). Resampling can be used to fill regular grid cells with DN value and write the final georectified image.

Suppose that $(j,\ k)$ is a pixel coordinate of a sample in the georectified image and $(x,\ y)$ is a geolocation of it in the regular grid. However, due to the repeated sampling and multi-scale sampling, the $(j,\ k)$ cell is covered by several pixels, just like Figure 8. How many DNs are there in the grid cell? The standard method is to return a DN of the nearest point to the grid cell, but it is not a suitable method.

By linear mixed pixel model, each part of a mixed pixel equals area ratio of the part and the whole pixel size [27].

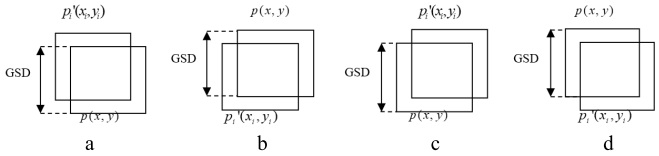

Fig. 9. The four cases of the pixel overlaps.

So the DN of $(j,\ k)$ cell, $\mathrm{g}'(j,k)$ is,

$$S = \sum_{i=1}^{n} w_i$$
$$g'(j,k) = \sum_{i=1}^{n} \frac{w_i}{S} g(x_i, y_i) \tag{5}$$

where, $\mathrm{g}(x_i, y_i)$ is the DN of ith pixel covering (i, j) cell, w_i is the weight of $\mathrm{g}(x_i, y_i)$ in the whole cell. We called the resampling model as linear mixed resampling model. Figure 8 shows the principle of a linear mixed resampling model.

There are four cases of (x_i, y_i) pixel covering (x, y) cell, shown in Figure 9.

According to Figure 9, the weight w_i of (x_i, y_i) is computed as follow.

(1) if $x_i \leq x$ and $y_i \leq y$, then

$$w_i = \frac{(x_i + GSD - x) \times (y_i + GSD - y)}{GSD \times GSD} \times \frac{1}{r_i} \tag{6}$$

(2) if $x_i \leq x$ and $y_i > y$, then

$$w_i = \frac{(x_i + GSD - x) \times (y + GSD - y_i)}{GSD \times GSD} \times \frac{1}{r_i} \tag{7}$$

(3) if $x_i > x$ and $y_i \leq y$, then

$$w_i = \frac{(x + GSD - x_i) \times (y_i + GSD_i - y)}{GSD \times GSD} \times \frac{1}{r_i} \tag{8}$$

(4) if $x_i > x$ and $y_i > y$, then

$$w_i = \frac{(x + GSD - x_i) \times (y + GSD_i - y_i)}{GSD \times GSD} \times \frac{1}{r_i} \tag{9}$$

where, r_i represents the scale size of the ith overlap pixel. The bigger r_i makes the spectra aliasing of the cell larger, at this time, w_i should be small.

C. The Processing Method of Missed Sampling

Large pitch angles result in some repeated samples, while others are not sampled. If the missed samples are not filled, there are some holes in the final image. In this paper, we tested four interpolation methods (Nearest neighbor, Inverse distance weighted, Bi-linear, and Cubic Catmull-Rom) [28], and test results are in Section 4.

IV. Experimentation and Analysis

A. Experiments 1: Time Sync Error Estimation

The implementation of the time sync error estimation is described in section 2.3 is presented here.

The HAA is a huge aerostat; the change of its position and orientation is very small in one second, so we set the time increment $\Delta \mathrm{t} = 1\mathrm{ms}$. General speaking, the timing offset $\Delta \mathrm{T}_{\mathrm{gps}}$ is small and less than 100 ms, so we can set the maximum number of the calculations M=100. We then choose a subset of hyperspectral image data including a linear feature (Figure 10) and select some pixels along the line, update the direct geo-coordinates of these pixels (see Section 2.3 for details) and compute the standard deviation of linear fitting of these pixel points until M=100, the standard deviations of linear fitting of 100 cycle times are shown in Figure 11. Finally, the timing offset $\Delta \mathrm{T}_{\mathrm{gps}}$ is calculated by multiplying the cycle index k corresponding the highest fitting precision and Δt, here $\Delta T_{gps} = 31ms$.

Fig. 10. The selected pixel points with linear features.

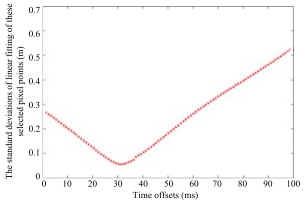

Fig. 11. The standard deviation of linear fitting of the selected pixel points corresponding to 100 groups of time sync data.

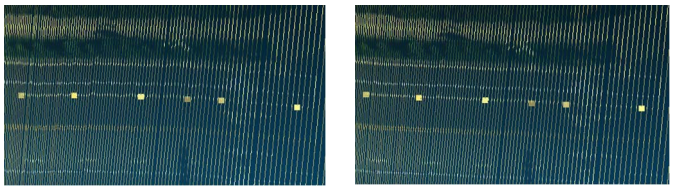

Fig. 12. The change of the feature line before and after the time sync error is estimated (Left: before the time sync error is estimated; Right: after the time sync error is estimated).

The results of the orthorectification of the hyperspectral image before and after time sync error estimation are shown in Figure 12. The results show that time sync error estimation is very important for push-broom imaging geocorrection.

B. Experiments 2: Resampling

In experiment two, we compared the nearest resampling method and our proposed resampling method; the comparison results are shown in Figure 13. Since several pixels cover a cell is not considered in the nearest resampling method, and the results of the nearest resampling method are not good.

The spectral similarity between two pixel points is used to evaluate the result of resampling quantitatively. Supposed that DNs of all bands of two pixels are $x_1, x_2, \cdots, x_n$ and

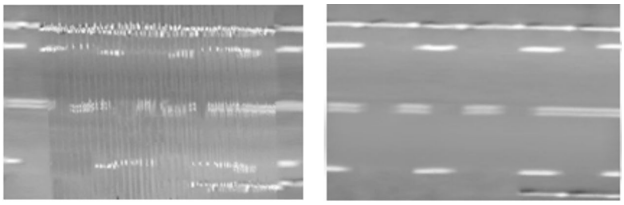

Fig. 13. The results of the different resampling methods (Left: the nearest resampling method; Right: our method).

TABLE II
THE COMPARISON RESULTS BETWEEN THE NEAREST RESAMPLING METHOD AND LINEAR MIXED RESAMPLING MODEL

Resampling methods	the average value of the similar spectral coefficients
nearest resampling	93.55%
linear mixed resampling model	98.96%

$y_1, y_2, \cdots, y_n$, the similar spectral coefficient is,

$$s = \frac{\sum_{i=1}^{n}(x_i - \overline{x})(y_i - \overline{y})}{\sqrt{\sum_{i=1}^{n}(x_i - \overline{x})^2 \sum_{i=1}^{n}(y_i - \overline{y})^2}} \tag{10}$$

where, $\bar{x}$ and $\bar{y}$ represent the average value of DNs of the pixel, s describes the similarity of the two pixels. If s is bigger; the two pixels are more similar.

In Figure 13, 100 similar spectral coefficients between original pixel points and resampling points were chosen, and the average value of them are listed in Table 2.

The comparative analyses from Figure 13 and Table 2 revealed that the linear mixed resampling model is superior to the nearest resampling method because the overlap and size of pixels are considered into our method.

C. Experiments 3: Comparison Analysis of four Interpolation Methods

An appropriate interpolation method should be chosen so that the "right" interpolated image data is filled into the missed samples. We compared four interpolation methods (Nearest Neighbor (NN), Inverse Distance Weighted (IDW), Bilinear (BL), and Cubic Catmull-Rom(CCR)) by qualitative and quantitative analysis.

Figure 14 is a subset of an enlarged image from each of four interpolation methods. It is clear that the result of the Bilinear interpolation is best, as it produces fewer jagged edges, and it does not introduce other apparent artifacts. However, the Cubic Catmull-Rom interpolation method produces some jagged edges and noise. The Cubic Catmull-Rom interpolation method is often used to enlarge images; the 16 nearest neighbors of the interpolated pixel should be smooth and continuous. When used with our hyperspectral imaging data, some nearest neighbors of the interpolated pixel are some missed sampling points, producing poor results.

The experimental results from the four interpolation methods were also evaluated by using average gradient.

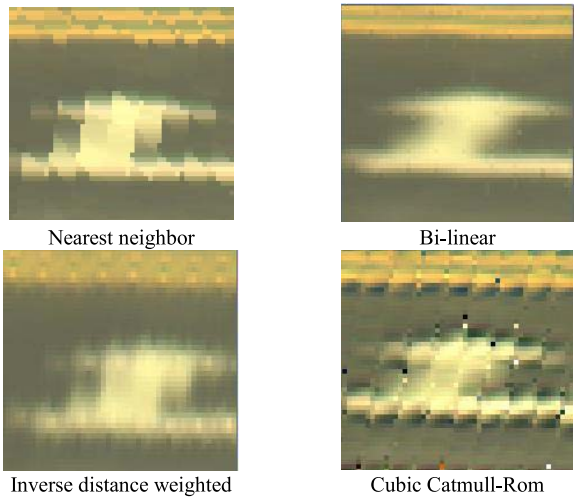

Fig. 14. Some local enlarged images from four interpolation methods.

TABLE III
THE AVERAGE GRADIENTS FROM FOUR INTERPOLATION METHODS

bands	Nearest neighbor	Bi-linear	Inverse distance weighted	Cubic Catmull-Rom
Red band	0.0052	0.0167	0.0049	0.0069
Green band	0.0051	0.0167	0.0048	0.0069
Blue band	0.0044	0.0139	0.0043	0.0065

The average gradient describes the image's clarity. A higher average gradient value indicates a better interpolation result. Red, green, and blue band images are interpolated separately using four interpolation methods, and their average gradients are calculated in Table 3. Table 3 shows that the average gradient of the bilinear interpolation is more than others. Bilinear interpolation is good for our hyperspectral imaging data to process the missed samples.

Interpolation can cause spectra aliasing, so an object classification test based on Maximum Likelihood is done to evaluate the spectra aliasing caused by the four interpolation methods. The two groups of the hyperspectral experiment data from the four interpolation methods were selected. One data set is from an urban area; another data set is from the water area. The test shows that the classification accuracy of the hyperspectral image processed by the Bilinear interpolation is the highest, on the other word, the Bilinear interpolation is best for hyperspectral imaging, in Table 4. The classification experiment and the average gradient test arrived at the same conclusion. The classification results of the corrected image by the Bilinear interpolation are shown in Figure 15 and Figure 16.

D. Experiments 4: Different Kinds of Remote Sensing Data Acquisition and Analysis

The ASQ-MPHAAS was tested on Jinyintan grassland with an average elevation of 3700m above the sea level. The different kinds of remote sensing data are captured at the same time when ASQ-MPHAAS navigated at an average altitude

TABLE IV

THE CLASSIFICATION ACCURACY OF THE HYPERSPECTRAL IMAGES PROCESSED BY THE FOUR INTERPOLATION METHODS

	urban area		water area	
	overall precision (%)	Kappa	overall precision (%)	Kappa
Nearest neighbour	76.3437	0.7233	88.9523	0.8742
Bilinear	91.9926	0.8957	97.1147	0.9568
Inverse distance weighted	74.6531	0.7125	85.4230	0.8261
Cubic Catmull-Rom	85.3894	0.8252	90.6038	0.8896

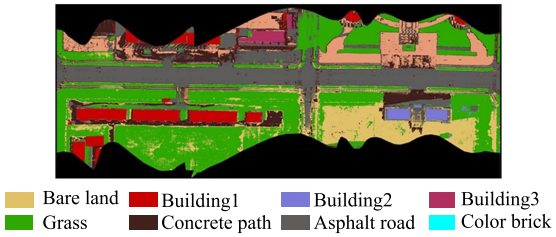

Fig. 15. The classification results of an urban area image.

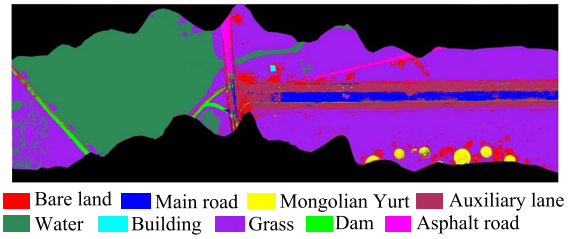

Fig. 16. The classification results of the water area.

of 300 m above ground. The main kinds of remote sensing data from ASQ-MPHAAS are described as follows.

1) Hyperspectral Image Data: To reduce development cost and the weight of the ASQ-MPHAAS, ASQ-MPOS-1 was directly installed under the ASQ-HAA having no three-axis stabilized platform. The large pitch angles and large roll angles appear due to the plateau airflow, and the orientation changes of the airship negatively affecting the push-broom images so that they are severely distorted as depicted in Figure 17③-1. We used Mark A.Warren's method [28], our geocorrection method [29] and the methods mentioned in Section 3 to correct the image (the results are shown in Figure 17). The image data in this test cover vegetation, building, or road areas and water areas. The spectra cover the spectral range of 389.882-1000.78 nm (VNIR) and 961.714 - 2581.48 nm (SWIR). The data were gathered at an average flight altitude of 300 m above ground with an average ground speed of 30 km/h, the ground resolution of the VNIR image is 0.094 m whereas the ground resolution of the SWIR image is 0.40 m.

2) Multi-Spectral Image Data: Four different band images are collected synchronously from the 4-camera multispectral imaging payload. Because the four cameras are independent,

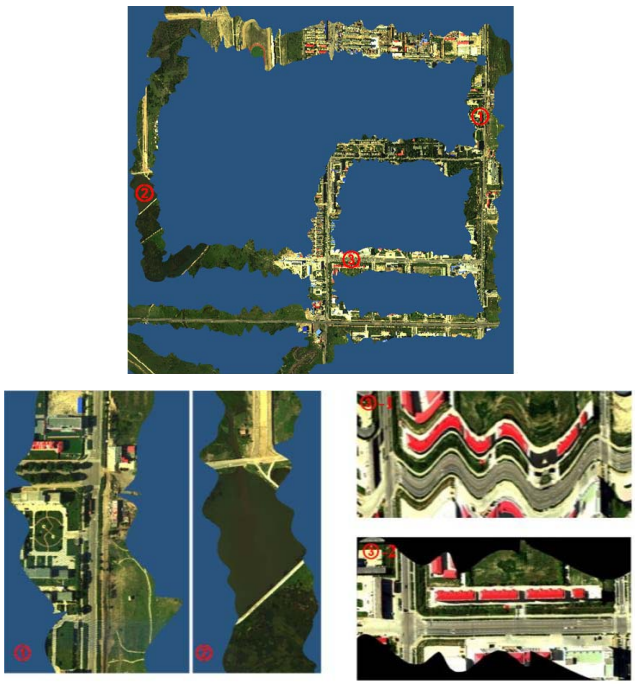

Fig. 17. Example hyperspectral image data are after geocorrection and resampling including vegetation, building, road and water areas.

they need to be aligned into a multispectral image. Image registration is essential for creating a multispectral image from 4-band images captured independently. In our research, the four band images of grassland were captured, but it is difficult to align the images because there are few manmade objects present. If the standard registration methods are employed, the results are unacceptable. Our research group proposed a geometry-windowing registration method for different band images of grassland based on 4-camera structure features [30], [31]. Figure 18 shows the individual images from the four cameras and the registration results. The registration error is less than 1.7 pixels if there are some artificial features, and the registration error is less than 2.8 pixels if there are not artificial features. The images were gathered at an average altitude of 300 m above ground; the ground resolution is 0.12 m, some sheep and cattle can be found in the final multispectral images.

3) The High-Resolution RGB Image: The high-resolution RGB images are captured by the Hasselblad 3DII-50 camera with 6132×8167 pixels. The Hasselblad 3DII-50 camera has a lens objective with a focal length of 50 mm; the ground resolution is 0.036m at an average altitude of 300 m above ground. The high-resolution RGB images can gather more details of objects. Here, they are used to detect the sheep and cattle (in Figure 19). Some applications for grassland livestock.

The technical data of the ASQ-MPHAAS is listed in Table 7. The ASQ-MPHAAS is a remote sensing monitoring system that is well suited to the plateau environment, and it can acquire high-resolution remote sensing data to meet the demands of different tasks.

For example, the ground resolution of the hyperspectral image data from the ASQ-MPHAAS is 0.094m @ 300m.

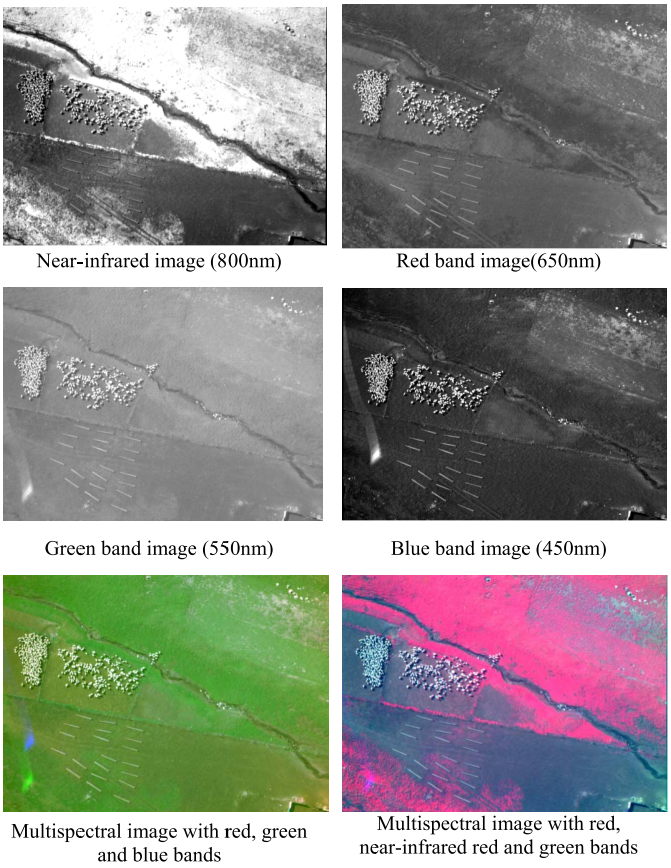

Fig. 18. Shows the individual images from the 4 cameras and the registration results.

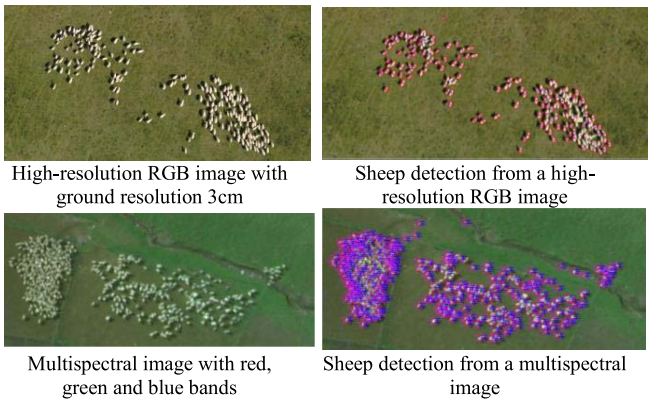

Fig. 19. Sheep detection from a high-resolution RGB image or multispectral image.

Different grass species can be distinguished using the hyperspectral data from the ASQ-MPHAAS, as seen in Figure 20. It is important for the scientific assessment of the grass nutritional status, distinguishing inedible grass from the forage and so on.

For another example, our research group employed the level set and morphology method to detect the sheep and cattle from these RGB images or the multispectral images, and calculated out the number and size of the sheep and cattle, in Figure 19. The accurate number of sheep and cattle is an important indicator of scientific grazing.

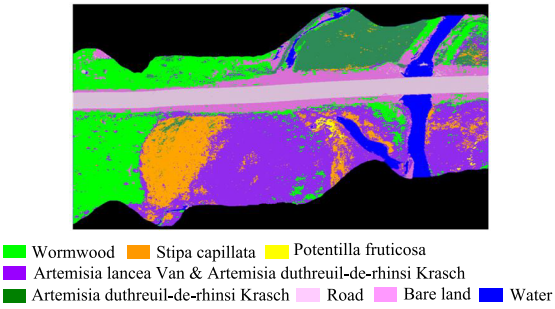

Fig. 20. Classification of different grass species using high-resolution hyperspectral images.

V. Conclusions

This study has described the design, implementation, and field trials of a multi-payload synchronized earth observation system from the high altitude airship (MPHAAS), which was developed for different high-resolution kinds of images acquisition. The multiple-task payloads consisting of two hyperspectral push-broom imaging payloads, a multispectral imaging payload, a high-resolution CCD camera, a video camera, a position and orientation system (POS), a time-synchronized control subsystem, and a power supply subsystem was integrated with ASQ-HAA380. A novel method for time-sync error estimation and a geometric correction workflow were proposed and implemented for the hyperspectral imagery. This study analyzed the characteristics of hyperspectral push-broom imaging when large pitch and roll angles appear alternately and a useful processing method for overcoming those issues. Four real-world field experiments were carried out to demonstrate the effectiveness of the ASQ-MPHAAS. The first experiment gave a processing workflow of time sync error estimation. It shows that time sync error impacts on the geocorrection. The second experiment and the third experiment demonstrated that the processing results of the special problems of hyperspectral push-broom imaging based on the ASQ-MPHAAS. A linear mixed resampling model proposed is to solve the multi-scale problem and repeat samples, and the Bi-linear interpolation is an appropriate method to solve the missed samples. The four experiments demonstrated that the ASQ-MPHAAS could be operated in the plateau environmental conditions. The hyperspectral image was corrected, and a multispectral image was created using the method proposed by our research group. The ASQ-MPHAAS simultaneously collected the four main kinds of the main remote sensing data including VNIR hyperspectral images, SWIR hyperspectral images, multispectral images, and RGB images; their ground resolutions are respectively 0.096m, 0.40m, 0.12m and 0.036m at an average flight altitude of 300 m above ground. These high-resolution remote sensing data has been used in the refined classification of grassland and the investigation of livestock.

We have demonstrated that the ASQ-MPHAAS is both possible and feasible on the plateau environmental conditions, resulting in high-resolution data products with unprecedented detail.

The ASQ-MPHAAS presented here opens up new opportunities for remote sensing monitoring of the plateau and other

ultrahigh-resolution remote sensing demand. In the future, we will continue to improve ASQ-MPHAAS's capabilities and data processing.

REFERENCES

[1] *Advanced Very High-Resolution Radiometer*. Accessed: Aug. 2019. [Online]. Available: https://gisgeography.com/avhrr-advanced-very-high-resolution-radiometer/?

[2] *MODIS*. Accessed: Aug. 2019. [Online]. Available: https://modis.gsfc.nasa.gov

[3] *Advanced Spaceborne Thermal Emission and Reflection Radiometer*. Accessed: Aug. 2019. [Online]. Available: http://terra.nasa.gov/about/terra-instruments/aster

[4] *Landsat 1-5 Multispectral Scanner*. Accessed: Aug. 2019. [Online]. Available: http://www.pcigeomatics.com/geomatica-help/references/gdb_r/landsat1-5.html

[5] *TM Satellite Sensor*. Accessed: Aug. 2019. [Online]. Available: http://landsat.usgs.gov/

[6] *ETM+ Satellite Sensor*. Accessed: Aug. 2019. [Online]. Available: http://landsat.usgs.gov/

[7] *Gaofen1,6(GF1,6)*. Accessed: Aug. 2019. [Online]. Available: https://space.skyrocket.de/doc_sdat/gf-1.htm

[8] C. Toth and G. Jóźków, "Remote sensing platforms and sensors: A survey," *ISPRS J. Photogramm. Remote Sens.*, vol. 115, pp. 22–36, May 2016.

[9] *DJ UAV*. Accessed: Aug. 2019. [Online]. Available: http://www.dji.com/

[10] A. Lucieer, Z. Malenovský, T. Veness, and L. Wallace, "HyperUAS—Imaging spectroscopy from a multirotor unmanned aircraft system," *J. Field Robot.*, vol. 31, no. 4, pp. 571–590, 2014.

[11] I. Colomina and P. Molina, "Unmanned aerial systems for photogrammetry and remote sensing: A review," *ISPRS J. Photogram. Remote Sens.*, vol. 92, pp. 79–97, Jun. 2014.

[12] *Airborne Topographic LiDAR—Leica Geosystems*. Accessed: Aug. 2019. [Online]. Available: https://leica-geosystems.com/en-us/products/airborne-systems/topographic-lidar-sensors

[13] *Lidar Systems—Teledyne Optech*. Accessed: Aug. 2019. [Online]. Available: http://www.teledyneoptech.com/index.php/products/airborne-survey/lidar-systems/

[14] *RIEGL Airborne Scanning*. Accessed: Aug. 2019. [Online]. Available: http://www.riegl.com/products/airborne-scanning/

[15] *Imaging Sensors*. Accessed: Aug. 2019. [Online]. Available: https://leica-geosystems.com/products/airborne-systems/imaging-sensors

[16] F. D. van der Meer *et al.*, "Multi- and hyperspectral geologic remote sensing: A review," *Int. J. Appl. Earth Observ. Geoinf.*, vol. 14, pp. 112–128, Feb. 2012.

[17] *Hyperspectral Imaging Cameras and Systems-Specim*. Accessed: Aug. 2019. [Online]. Available: http://www.specim.fi

[18] R. Hruska, J. Mitchell, M. Anderson, and N. F. Glenn, "Radiometric and geometric analysis of hyperspectral imagery acquired from an unmanned aerial vehicle," *Remote Sens.*, vol. 4, no. 9, pp. 2736–2752. 2012. doi: 10.3390/rs4092736.

[19] N. Oppelt and W. Mauser, "Airborne visible/infrared imaging spectrometer AVIS: Design, characterization and calibration," *Sensors*, vol. 7, no. 9, pp. 1934–1953, 2007. doi: 10.3390/s7091934.

[20] A. Abd-Elrahman, R. Pande-Chhetri, and G. Vallad, "Design and development of a multi-purpose low-cost hyperspectral imaging system," *Remote Sens.*, vol. 3, no. 3, pp. 570–586, 2011. doi: 10.3390/rs3030570.

[21] J. Kelcey and A. Lucieer, "Sensor correction of a 6-band multispectral imaging sensor for UAV remote sensing," *Remote Sens.*, vol. 4, no. 5, pp. 1462–1493, 2012. doi: 10.3390/rs4051462.

[22] *SPAN- CPT*. Accessed: Aug. 2019. [Online]. Available: https://www.novatel.com/assets/Documents/Papers/SPAN-CPT.pdf

[23] *IEEE 1588 Precision Time Protocol (PTP) Version 2 Specification*, IEEE Standard 1588-2008, Mar. 2008

[24] D. L. Mills, *Network Time Synchronization—The Network Time Protocol on Earth and in Space*. Boca Raton, FL, USA: CRC Press, 2011, p. 466.

[25] D. Mills, *Network Time Protocol Version 4 Protocol and Algorithms Specification*. document RFC 5905, Internet Engineering Task Force, Jun. 2010.

[26] *Altera and IDT Synchronous Ethernet Solution for ITU-TG.8262 White Paper*. Accessed: Aug. 2019. [Online]. Available: https://www.intel.com/content/dam/www/programmable/us/en/pdfs/literature/wp/wp-01256-altera-and-idt-synchronous-ethernet-solution-for-itu-t-g8262.pdf

[27] C. Dey, X. Jia, D. Fraser, and L. Wang. "Mixed pixel analysis for flood mapping using extended support vector machine," in *Proc. Digit. Image Comput. Techn. Appl.*, Dec. 2009, pp. 291–295. doi: 10.1109/DICTA.2009.55.

[28] M. A. Warren, B. H. Taylor, M. G. Grant, and J. D. Shutler, "Data processing of remotely sensed airborne hyperspectral data using the Airborne Processing Library (APL): Geocorrection algorithm descriptions and spatial accuracy assessment," *Comput. Geosci.*, vol. 64, pp. 24–34, Mar. 2014.

[29] A. Zhang, S. Hu, X. Meng, L. Yang, and H. Li, "Toward high altitude airship ground-based boresight calibration of hyperspectral pushbroom imaging sensors," *Remote Sens.*, vol. 7, no. 12, pp. 17297–17311, 2015. doi: 10.3390/rs71215883.

[30] H. Li, A. Zhang, and S. Hu, "A multispectral image creating method for a new airborne four-camera system with different bandpass filters," *Sensors*, vol. 15, no. 7, pp. 17453–17469. doi: 10.3390/s150717453.

[31] H. Li, A. Zhang, and S. Hu, "A registration scheme for multispectral systems using phase correlation and scale invariant feature matching," *J. Sensors*, vol. 2016, Nov. 2015, Art. no. 3789570. doi: 10.1155/2016/3789570.

Shaoxing Hu received the Ph.D. degree in mechanical-electronic engineering from Jilin University, Jilin, China, in 2001.

From 2002 to 2004, he held a post-doctoral position with the National Key Laboratory on Machine Perception, Peking University, Beijing, China. He is currently an Associate Professor with the School of Mechanical Engineering and Automation, Beihang University, Beijing, China. His research interests include remote sensing sensor design and development, computer vision and image processing, and lidar SLAM.

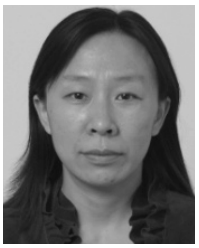

Aiwu Zhang received the Ph.D. degree from Jilin University, Jilin, China, in 2002. Her Ph.D. research focused on computer vision and image processing.

From 2002 to 2004, she held a post-doctoral position with the Department of Electronic Engineering, Tsinghua University, Beijing, China. She is currently a Professor with the Ministry of Education Key Laboratory of 3D Information Acquisition and Application, Capital Normal University, Beijing. Her research interests include remote sensing image processing, computer vision, hyperspectral/multispectral imaging, and lidar 3D mapping.

Shatuo Chai is currently an Associate Professor with the Qinghai Academy of Animal Science and Veterinary, Qinghai University, Qinghai, China. His research interests focus on the nutrition balance of grass and livestock.